

Pack Aluminization Synthesis of Superalloy 3D Woven and 3D Braided Structures

DINC ERDENIZ, AMANDA J. LEVINSON, KEITH W. SHARP,
DAVID J. ROWENHORST, RICHARD W. FONDA, and DAVID C. DUNAND

Micro-architected, precipitation-strengthened structures were created in a new process combining weaving, gas-phase alloying, diffusion, and precipitation. First, high-ductility Ni-20 wt pct Cr wires with 202 μm diameter were braided, or non-crimp orthogonal woven, into three-dimensional structures. Second, these structures were vapor-phase alloyed with Al at 1273 K (1000 °C) by pack cementation, creating uniform NiAl coatings on the wires when using a retort. Also, solid-state bonding was achieved at wire intersections, where two wires were sufficiently close to each other, as determined *via* optical and X-ray tomographic microscopy. Third, the NiAl-coated wires were fully homogenized and aged to form γ' precipitates distributed in a γ matrix phase, the same microstructure providing strength in nickel-based superalloys. The resulting structures—consisting of wires (i) woven in a controlled three-dimensional architecture, (ii) bonded at contact points and (iii) strengthened by γ' precipitates—are expected to show high strength at ambient and elevated temperatures, low density, and high permeability which is useful for active cooling.

DOI: 10.1007/s11661-014-2602-9

© The Minerals, Metals & Materials Society and ASM International 2014

I. INTRODUCTION

PERIODIC cellular metals share desirable properties with stochastic metal foams such as low density, and high specific strength, stiffness, sound absorption, damping, and surface area.^[1–9] Furthermore, periodic cellular metals can be micro-architected to optimize various properties in an isotropic or anisotropic manner, which cannot be achieved with porous or foamed metals due to their irregular structures.^[10,11] Some examples of periodic cellular materials are honeycombs,^[2,3] trusses,^[3–5] and assembly of helical wires,^[6,7] which can all be used as the core of sandwich structures. Fabrication of such periodic structures from high-temperature alloys is highly desirable: for instance, cellular Ni-based superalloys could reduce the mass of jet engine parts while enabling efficient cooling which may enable increased operating temperature of the engine. Also, topologically tailored micro-architectures can be designed using optimization tools which offer, for example, optimized combination of high strength/stiff-

ness and high heat transfer properties for thermo-structural applications.^[12–14] However, there are severe limitations for the fabrication of such structures from high-strength superalloys with limited ductility, due to difficulties in cutting, shaping, and joining these high temperature alloys. A small number of studies report the production of periodic cellular superalloys,^[15–17] none using property optimization tools. Nathal *et al.*^[15] used investment casting to produce IN718 truss panels with 1.5 mm diameter struts and assembled them *via* hot isostatic pressing (HIP). Zhang and He^[16] brazed honeycomb structures from corrugated 90 μm thick Ni-based alloy sheets. Murr *et al.*^[17] created IN625 mesh structures with 0.6 to 1 pore per millimeter *via* additive manufacturing, using electron beam melting. To the best of our knowledge, there are no reports on the fabrication of woven or braided structures from superalloy wires, due to three significant manufacturing difficulties: (i) commercial superalloy wires are difficult to draw due to their limited ductility and are thus not widely available, especially below ~ 500 μm diameter; (ii) when available, these superalloy wires are not sufficiently ductile at room temperature to withstand the necessary bending angles for weaving; and (iii) bonding of 3D woven superalloy wires is challenging.

We take here a novel approach to overcome these issues by inverting the established sequence of the manufacturing steps of (i) wire alloying, (ii) wire weaving/braiding, and (iii) wire bonding. Specifically, we use ductile Ni-20 wt pct Cr precursor wires to weave or braid complex structures and subsequently aluminize, homogenize, and age the wires to achieve superalloy microstructures with γ' precipitates, while also creating bonds at wire contact points. A similar in situ alloying approach was previously applied to other metals, where pure Ni LIGA

DINC ERDENIZ, Postdoctoral Fellow, and DAVID C. DUNAND, James N. and Margie M. Krebs Professor, are with the Department of Materials Science and Engineering, Northwestern University, 2220 Campus Drive, Evanston, IL 60208. Contact e-mail: d-erdeniz@northwestern.edu AMANDA J. LEVINSON, Postdoctoral Research Associate, is with the National Research Council Fellow US Naval Research Laboratory, 4555 Overlook Avenue SW, Washington, DC 20375. KEITH W. SHARP, Product Manager, is with the 3D Fabrics, SAERTEX USA, LLC, 2200-A Mt. Holly-Huntersville Road, Huntersville, NC 28078. DAVID J. ROWENHORST, Materials Research Scientist, and RICHARD W. FONDA, Head, are with the Micro-structural Evolution and Joining Section, US Naval Research Laboratory, 4555 Overlook Avenue SW, Washington, DC 20375.

Manuscript submitted May 27, 2014.

Article published online October 18, 2014

objects were alloyed with Al^[18] and pure Ni foams were alloyed with Al,^[19,20] Cr,^[20–22] and Fe^[22] by pack cementation, a chemical vapor deposition process that creates uniform coatings on metal parts^[23] and is widely used to form aluminate surface layers on commercial Ni-based superalloys.^[24,25] The part to be pack cemented is buried in a powder mixture (the pack) consisting of a filler (usually Al₂O₃), an activator (a halide salt), and a metal source (pure or in alloy form). At elevated temperature, the activator decomposes and reacts with the source to create a metal halide gas, which subsequently deposits the metal on the substrate surface. The deposited metal diffuses into the substrate and forms a coating, which usually extends a few tenths of millimeters into the part. In cemented Ni foams, complete homogenization of the alloying elements is achievable by annealing after deposition as a coating on the struts of the foam, resulting in homogeneously alloyed struts after heat-treatment.^[19–22] The same approach (pack aluminization followed by complete homogenization) was used to add Al to various Ni-based alloy (IN-625, IN-693, H-214, X-750) sheets, with thicknesses between 0.2 and 1 mm, to achieve precipitation strengthening for potential use in thermostructural panels.^[26] A prior study on the aluminization of individual Ni and Ni-20 wt pct Cr wires, identical to those used in the present research, is reported elsewhere.^[27]

We report here the creation of γ/γ' precipitation-strengthened, 3D architected, wire structures by a multi-step process consisting of first braiding or weaving ductile Ni-20 wt pct Cr wires and then alloying, bonding, homogenizing, and aging the wire structures. The macro/microstructural evolution during the alloying and heat-treatment steps is investigated *via* optical, electron, and X-ray tomographic microscopy as well as micro-hardness measurements.

II. EXPERIMENTAL PROCEDURES

A. 3D Braiding and 3D Weaving

Three types of specimens were created: one 3D braided tube and two non-crimp 3D orthogonal woven structures with two different micro-architectures. 3D braiding intertwines the wires so that there is no true layering in the structure, providing integral, out-of-plane reinforcement with integral, multidirectional wire reinforcements.^[28–32] The wire architecture is non-orthogonal and typically incorporates four sets of intertwined wires oriented at the same angle to the longitudinal (fabric formation) axis. In addition, longitudinal wires oriented in the fabric formation direction can be incorporated. Wire architecture of this kind of 3D braid is illustrated in Figure 1(a). A novel 3D rotary braiding process was used to produce the forms in this research. The motion of the braiding carrier involves circular horn gears that each holds four carriers of wire and fork gears at each 90 deg location on the horn gear that transfer the wire carriers between horn gears. This innovative, patented method of wire carrier transfer between horn gears allows all horn gear positions to be

occupied by wire carriers.^[33] The transfer between the rotating horn gears is swift and computer-controlled, as is the synchronization with the take-up of the braid. This process allows each carrier location in the machine to be fully occupied, resulting in a relatively small bedplate size that can operate at high speed, and it can alter the braiding pattern, and thus shape of the braided form, without stopping the machine.^[31,32] The machine used here has the capability to use up to 576 braided wire ends and 144 axial wire strands.

Using soft-annealed Chromel A wires (Ni-20 wt pct Cr-1 wt pct Si-0.05 wt pct Fe, labeled Ni-20Cr from here on) with a diameter of 202 μm (32 gage), 160 carriers of the 3D braiding machine were loaded to form a tubular shape. With a take-up of 1.8 mm per cycle, four 200 mm lengths of 3D braided Ni-20Cr were manufactured as a tube.

In orthogonal 3D weaves, the through thickness (z -) wires are perpendicular to the plane of the fabric, as shown in Figure 1(b), and hold the fabric together. Heddles reposition the Z wires on each machine cycle after the fill (y -) wire insertion. Using a patented multi-rapier fill insertion process,^[28,29] all layers are simultaneously woven in a single machine cycle. In the resultant wire architecture, the warp (x -) wires do not bend, only advance linearly with each machine cycle. The fill (y -) wires also lay un-crimped through the fabric, then bend only outside the edge of the fabric. The Z wires remain approximately vertical with respect to the plane of the fabric within the fabric, and then complete a 180 deg turn around the outermost fill-wire at each surface to return through the fabric to bind the weave together.

Using the same Ni-20Cr wires, a set of 30 mm wide, 3.2 mm thick specimens were 3D woven on a small multi-rapier insertion 3D weaving machine. The base architecture, labeled “standard weave” from here on, shown in Figure 1(c), can be described as follows:

- Five layers in warp (length) and six layers in fill (width);
- For each warp layer, two wires are placed at a spacing of 15.7 locations per cm across the width;
- For each fill layer, two wires are placed at a spacing of 12.5 locations per cm (0.7 mm per insertion) along the length;
- Single Z wires are aligned with the warp wires, spaced at 15.7 locations per cm across the width and inserted through the thickness 12.5 times per cm along the length.

To produce the optimized architecture, labeled “optimized weave” from here on and shown in Figure 1(d), all of the surface wire positions are filled, but alternating columns of interior warp layers (layers 2 to 4) across the width are left vacant and alternating positions of interior fill layers are left vacant (layers 2 and 4, then layers 3 and 5).

B. Pack Aluminization and Heat-Treatment

A pack mixture—labeled P50 following the nomenclature employed in Reference 27—was used, consisting

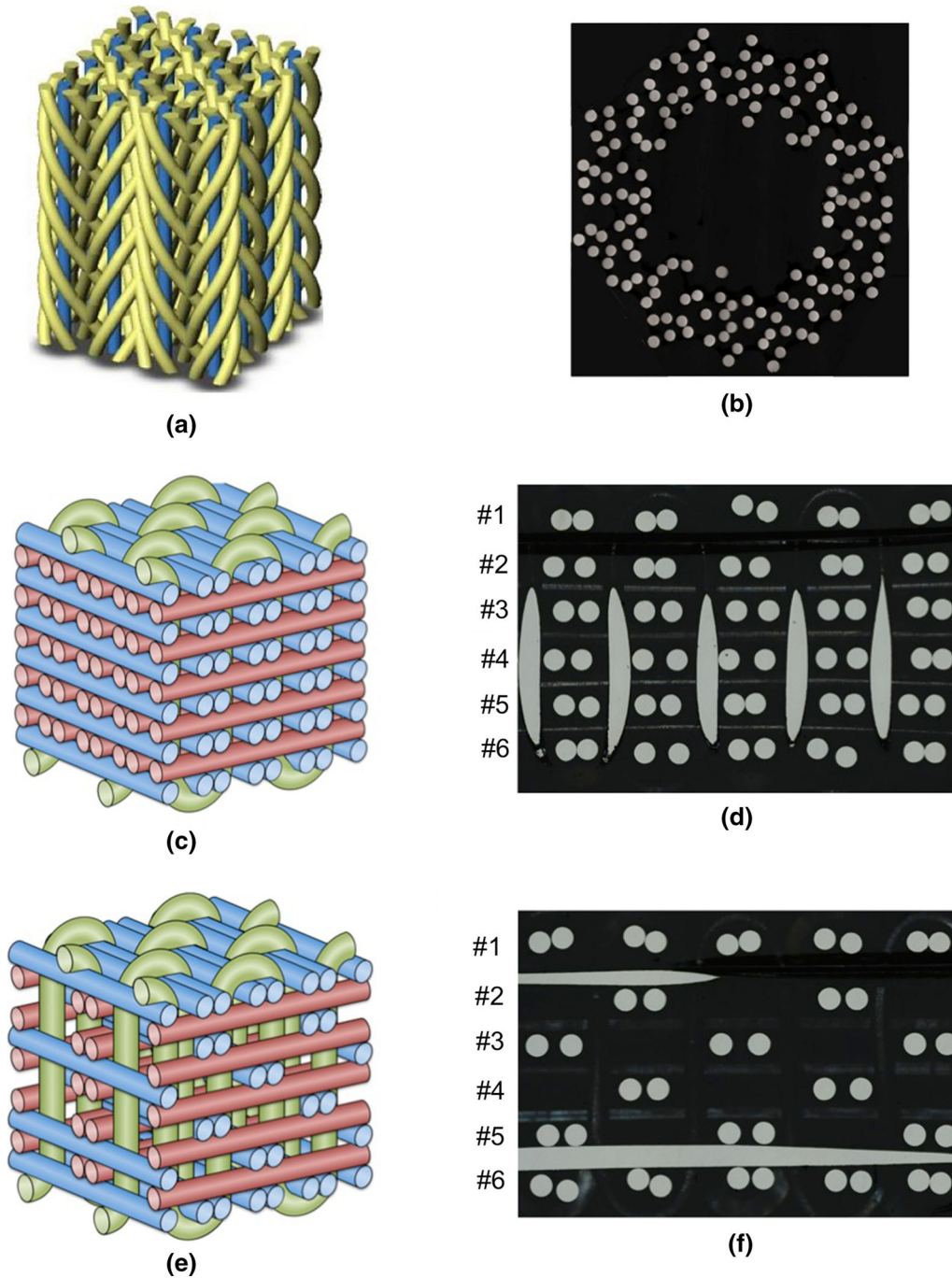


Fig. 1—(a) Schematic of the 5-directional fiber architecture in a generic 3D braid, (b) Optical micrograph showing the cross-section of a tube braided based on the architecture given in (a), (c) Schematic of the orthogonal 3D weave fiber architecture with the standard configuration where all wire positions are filled. Red wires are warp, blue are fill, and green are Z, (d) Optical micrograph showing the cross-section (warp–z) of a standard weave, (e) Schematic of the orthogonal 3D weave fiber architecture with the optimized configuration where alternating wire positions are left empty in warp and fill directions. Red wires are warp, blue are fill, and green are Z, (f) Optical micrograph showing the cross-section (warp–z) of an optimized weave (Color figure online).

of 82 wt pct Al_2O_3 powders (20 to 50 μm particle size, procured from Alfa Aesar), 15 wt pct of Raney Ni precursor powders (Ni-50 wt pct Al, 150 μm particle size, procured from Alfa Aesar), and 3 wt pct NH_4Cl powders (100 μm particle size, procured from Alfa Aesar). A quantity of 25 g of pack was poured in either an Al_2O_3 crucible (for experiments under atmospheric

pressure, reported as non-pressurized aluminization) or a stainless steel retort, where the gas pressure rises at elevated temperatures (for experiments under increased pressure for better gas penetration into the samples, reported as pressurized aluminization). Inner surfaces of the steel retorts were spray-coated with boron nitride to minimize contamination. As-received specimens were

cut and ultrasonically cleaned in acetone. After air-drying at ~ 373 K (100 °C), two samples were buried in the pack. The container (alumina crucible or steel retort) holding the pack and the samples was placed at the water-cooled end of a tube furnace that was preheated to 1273 K (1000 °C). After flushing the tube for 15 minutes with Ar, the container was pushed into the hot zone of the furnace and held there for 30, 60, 90, and 120 minutes. It was then pulled back to the water-cooled end and cooled in that position for 15 minutes. The aluminized specimens were then ultrasonically cleaned in acetone to remove the pack remnants and weighed to determine the amount of Al added. Select samples were encapsulated in quartz tubes under vacuum, homogenized at 1473 K (1200 °C) for 48 hours and aged at 1173 K (900 °C) for 8 hours. All heat treatments were terminated by water quenching.

C. Metallography, Microscopy, and Hardness Testing

Samples were mounted in epoxy and prepared for microscopy *via* standard metallographic techniques. An etchant composed of 33 vol pct deionized water, 33 vol pct acetic acid, 33 vol pct nitric acid, and 1 vol pct hydrofluoric acid was used to reveal γ' precipitates in the aged samples. A scanning electron microscope (SEM) equipped with an energy dispersive X-ray spectrometer (EDS) was used for imaging and chemical analyses. The EDS signal was calibrated by using standard samples of Ni_2Al_3 and Ni-20 wt pct Cr.

Micro-Vickers hardness tests were conducted on polished cross-sections with a Struers Duramin 5 hardness tester by applying a 136 deg pyramidal diamond indenter under a load of 100 g for 10 seconds. At least five measurements were taken for each sample and the average value is reported.

D. Image Acquisition and Reconstruction using X-ray Micro-Computed-Tomography

X-ray micro-computed-tomography was performed on four Ni-20 wt pct Cr wire weaves to quantify the degree of bonding between different vapor-phase alloying conditions. The four optimized weaves examined had mass gains of either 6 or 8 wt pct Al from the pack aluminization and were evaluated in both the non-homogenized and homogenized states. The weaves were infiltrated with slow-curing epoxy under vacuum to prevent wire fallout during sectioning. Samples with a cross-section of 1.5×1.5 mm² were sectioned from the center of the weave along the warp direction to achieve a spatial resolution of 1.77 $\mu\text{m}/\text{pixel}$ and minimize beam hardening from high-density layers.

X-ray tomography was conducted with a Sky-Scan1172 high-resolution micro-CT, using a micro-positioning stage to achieve proper sample alignment. A 100 kV, 10 W polychromatic X-ray point source with an 11 Mp, 12-bit cooled CCD detector was used to produce X-ray transmission images. The total scanned volume per sample was approximately $1.5 \times 1.5 \times 6.6$ mm³.

Data reconstruction was performed using the Sky-Scan NRecon software package that employs the Feldkamp algorithm.^[34] Image segmentation to distinguish the wires was performed using the expectation-maximization/maximization of the posterior marginals (EM/MPM) algorithm.^[35] This is a texture-based local thresholding technique that uses Bayesian statistics to minimize the number of misclassified pixels in the structure, and it excels at segmenting noisy or textured images. To alleviate memory demands during image segmentation and subsequent analysis of bonding efficiency, the datasets were down-sampled, resulting in a final voxel size of 3.54 μm^3 .

III. RESULTS AND DISCUSSION

A. Fabrication

The final optimized non-crimp 3D orthogonal woven part had an average 3.2 mm thickness, and the fill insertion spacing was 0.7 ± 0.02 mm. The metal volume fraction was 11.6 pct in the warp, 12.0 pct in the fill, and 9.1 pct in the Z directions for a total metal volume fraction of 32.7 pct.

Table I summarizes the aluminization results in terms of weight gain and final Al concentration for three different wire architectures (standard weave, optimized weave, braided tube), four different aluminization times (30, 60, 90, 120 minutes), and two different aluminization methods (pressurized, non-pressurized). After 60 minutes of aluminization, braided tubes, standard weaves, and optimized weaves exhibited mass gains corresponding to average aluminum compositions of 5.7 ± 0.2 , 3.9 ± 0.1 , and 5.3 ± 0.3 wt pct Al, respectively. For longer times, the aluminum content increases, but the pack was fully consumed in ~ 2 hours. For the shorter 30 minutes aluminization, all samples exhibited Al contents insufficient to ensure the formation of γ/γ' microstructure upon homogenization and aging. Therefore, we only report on the samples aluminized for 60 minutes from this point on, given that their overall Al content after homogenization is expected to result in a γ/γ' microstructure.

Coating thickness was uniform throughout the braided sample, but, for the two weaves, it was wider in wires near the sample surface, and narrower for those close to the sample core. This indicates that the wires near the core were partially shielded from the halide gas, and thus aluminized more slowly than those near the surface. This shielding effect can be expected to be reduced in the optimized samples whose core is more open to the gas *via* the channels created by the removal of wires. This is consistent with the observed trend of faster aluminization for the optimized weaves than for the standard weaves.

Pressurized aluminization for 60 minutes resulted in Al mass gains of 4.3 ± 0.3 and 4.8 ± 0.2 wt pct Al for standard and optimized weaves, respectively. A uniform coating thickness was achieved on all wires within the weave, indicating that gas gradients were absent. Within error, the aluminization rates were the same.

Table I. List of All Conditions Applied for the Aluminization of 3D Woven and 3D Braided Ni-20Cr Structures

Specimen Type	Pack Type	Time (min)	Mass Gain (mg)	Al Concentration (wt pct)
Standard weave	non-pressurized	30	25 ± 4	3.0 ± 0.1
Standard weave	non-pressurized	60	33 ± 4	3.9 ± 0.1
Standard weave	non-pressurized	90	42 ± 4	5.0 ± 0.3
Standard weave	non-pressurized	120	35 ± 8	5.0 ± 0.2
Standard weave	pressurized	60	50 ± 1	4.3 ± 0.3
Optimized weave	non-pressurized	30	20 ± 4	3.4 ± 0.4
Optimized weave	non-pressurized	60	29 ± 6	5.3 ± 0.3
Optimized weave	non-pressurized	90	33 ± 2	5.9 ± 0.3
Optimized weave	non-pressurized	120	35 ± 2	6.5 ± 0.1
Optimized weave	pressurized	60	41 ± 1	4.8 ± 0.2
Braided tube	non-pressurized	60	64 ± 5	5.7 ± 0.2
Braided tube	pressurized	60	70 ± 3	5.6 ± 0.2

For each condition three specimens were prepared.

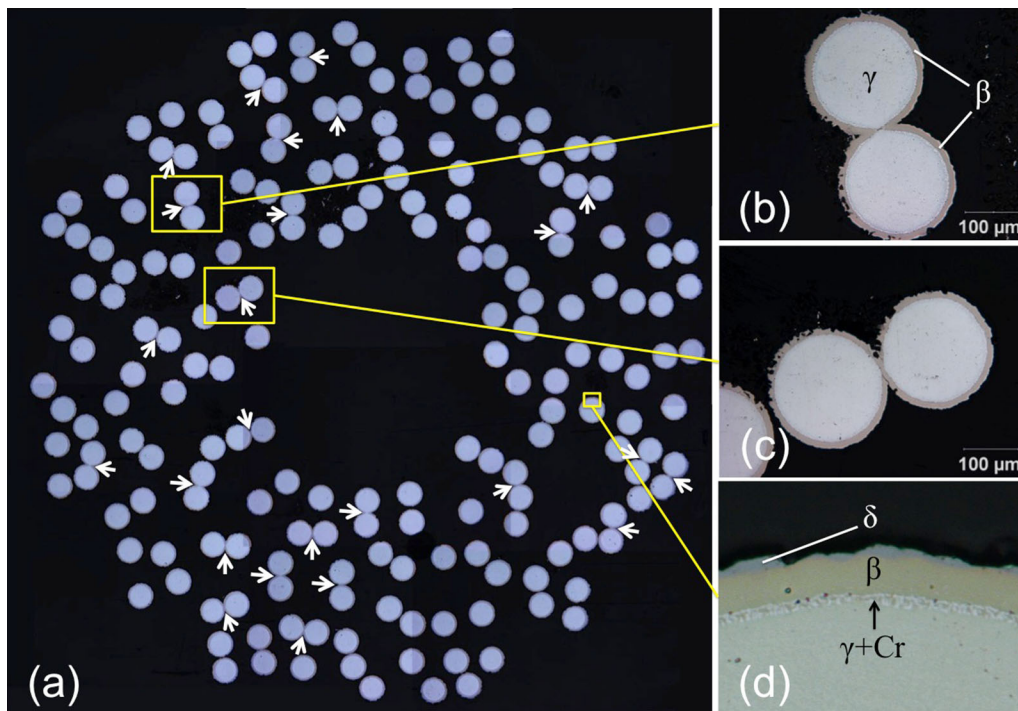


Fig. 2—(a) Braided structure after non-pressurized aluminization at 1273 K (1000 °C) for 1 h, (b through c) showing wires bonded to each other via the merging of β -NiAl coating layers, (d) an α -Cr rejection layer is visible at the β -NiAl/ γ -Ni-20Cr interface. Also visible is a thin, discontinuous δ -Ni₂Al₃ layer at the surface of the wire.

B. Microstructure

Figure 2(a) shows the cross-section of a braided tube aluminized under non-pressurized conditions. The wires shown in Figures 2(b) through (d) have $12 \pm 1 \mu\text{m}$ thick coatings of NiAl phase and thin discontinuous surface layers of Ni₂Al₃ phase, Figure 2(d), which are relatively uniform throughout the sample. The coating thickness uniformity is crucial to the fabrication of samples with uniform compositions. Between the NiAl shell and the Ni-20Cr core, a layer rich in Cr is visible, which is rejected from the growing NiAl shell during the aluminization process. A similar observation was made for individual Ni-20Cr wires aluminized in a lower activity

pack (P40, Al source: Ni-40 wt pct Al).^[27] The formation of the NiAl phase is, however, inconsistent with the results obtained in the previous study conducted with individual wires,^[27] where a P50 pack (Ni-50 wt pct Al), also used in the present work, resulted in the formation of Ni₂Al₃ coatings and much faster aluminization kinetics. However, there are previous reports that suggest that packs similar to P50 can indeed create NiAl coatings.^[20,25] The discrepancy seems to be due to the total mass of the samples in the pack: as the total surface of Ni wires increases, the kinetics of aluminide formation slow down due to the fixed amount of Al present in the pack.

An important observation for both non-pressure and pressure aluminized samples is that some bonding was achieved at the wire contact points. During aluminization, the diameter of the wires increases due to the deposition of Al and formation of NiAl: for 4 to 6 wt pct Al addition, the wire radius increases by ~2 to 5 μm , based on measurements taken from micrographs and assuming a constant 202 μm starting diameter. The NiAl coatings were found to encase seamlessly the regions where two wires were in contact or very close to each other, thus creating a metallurgical bond between the wires, as marked with arrows in Figure 2. Although in most cases the joint area is small compared to the wire cross-section, the bonding may lead to considerable increase in stiffness and strength of the weave, which can be further improved by subsequent application of liquid phase sintering or brazing.

For all the micrographs of the woven structures given here, Figures 3, 4, 5, and 6, the radial wire cross-sections are the fill couples (six layers), the horizontal wires are the warps (five layers), and the Z-wire loops, aligned with the warp wires, are partially visible in some of the images depending on the location of the final polished cross-section. Figure 3(a) shows the cross-section of a standard weave aluminized under non-pressurized conditions. A 10 μm NiAl shell is visible on both surface fill layers (#1 and #6), the thickness decreases to 8 μm on the second layers (#2 and #5) and there is almost no

coating visible on the two layers at the center of the weave (#3 and #4), as seen in Figures 3(b) through (d). The standard architecture is the most closely packed one among the three configurations reported here. This clearly shows that the gas penetration at atmospheric pressure is very limited in the core of the sample and does not supply sufficient Al halides to the inner wires of the sample. Figure 3(b) shows an example of solid-state bonding between two adjacent wires. The NiAl coating on both wires grew, impinged and merged. The bond length is 45 μm and sharp cusps are visible at the edge of the bonded region, indicating that surface diffusion is slow compared to Al deposition speed.

Figure 4(a) shows the cross-section of a standard weave that was aluminized under pressurized conditions. It is clearly seen in Figures 4(b) through (d) that the coating thickness, ~10 μm , is very uniform throughout the sample with an average decrease of only ~10 pct in the coating thickness from the surface layers to the central layers. The retort prevents the gas loss during the process, hence increases the partial pressure of the halides. This results in a much more uniform coating than the non-pressurized coating, where the crucible lid only partially prevents gas loss. Increased halide partial pressures did not result in faster kinetics of aluminization as the coating formation is diffusion controlled, and its kinetics solely depend on the surface Al concentration. In this case, the coating still consisted of the NiAl

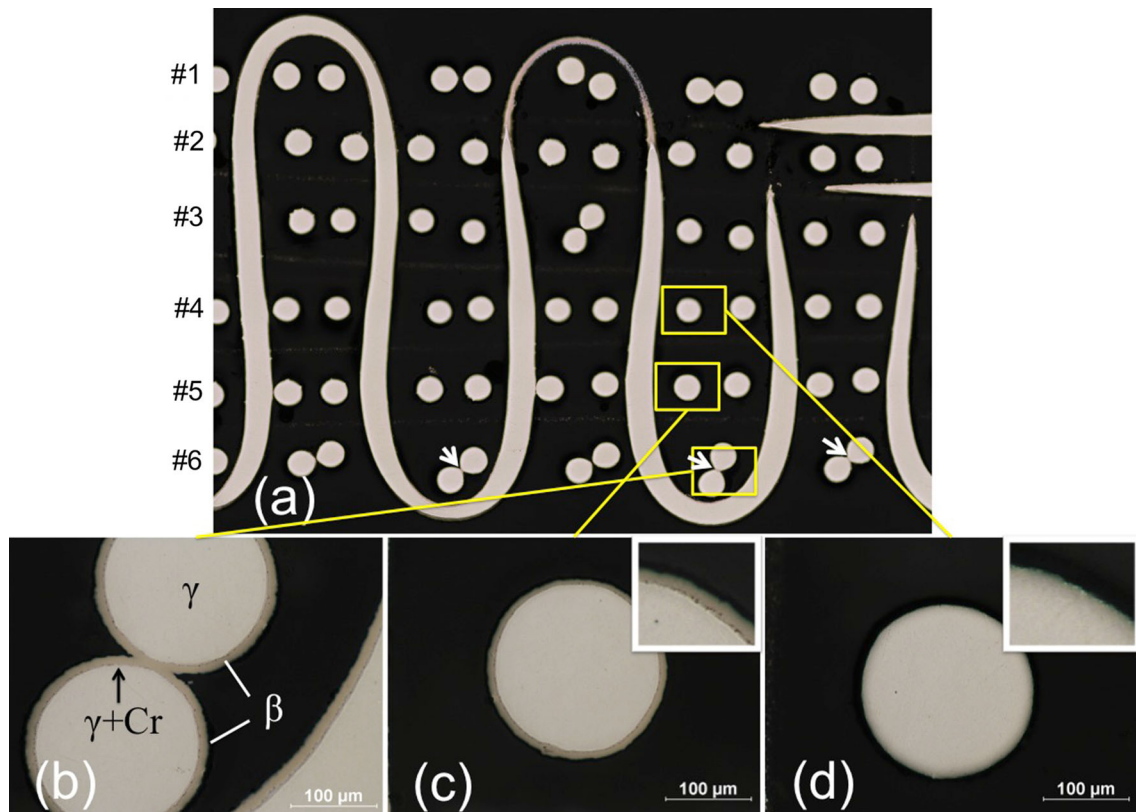


Fig. 3—(a) Standard woven structure after non-pressurized aluminization at 1273 K (1000 °C) for 1 h, (b through d) showing higher magnification images of wires in various regions of the sample, where the β -NiAl coating becomes thinner on the inner layer of the sample. An α -Cr rejection layer is present at the β -NiAl/ γ -Ni-20Cr interface. Wire bonding is observed in (b) where NiAl coatings merged during their growth. Insets in (c) and (d) show the thickness of the coatings at a higher magnification.

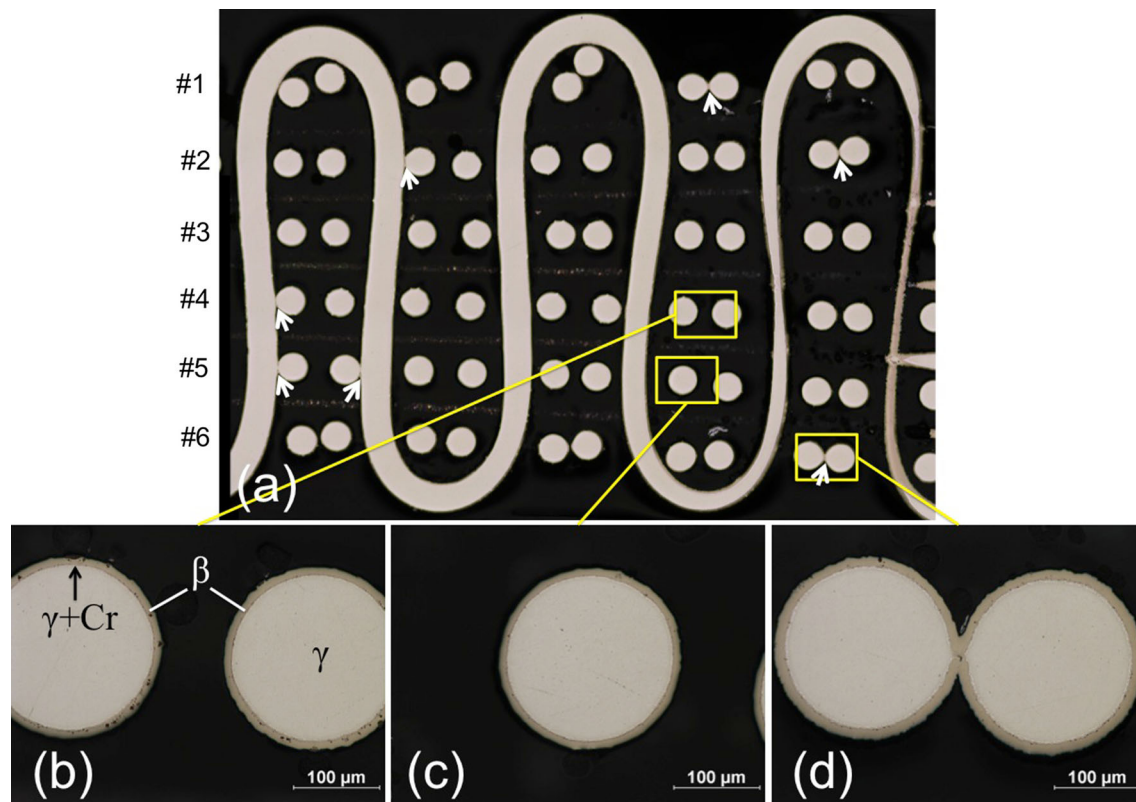


Fig. 4—(a) Standard woven structure after pressure aluminization at 1273 K (1000 °C) for 1 h. (b through d) showing higher magnification images of wires in various regions of the sample, where the β -NiAl coating has a uniform thickness. An α -Cr rejection layer is present at the β -NiAl/ γ -Ni-20Cr interface. Wire bonding is observed in (d) where NiAl coatings merged during their growth.

phase, hence the surface Al concentration or the aluminization kinetics did not change significantly as compared to the non-pressurized aluminization. Figure 4(d) shows bonding between two wires, where the bonded region is 40 μm in length. There is a small gap at the center of the bond, possibly due to incomplete merging of the coatings. As also observed in the bond region shown in Figure 3(b), sharp cusps are present.

Figure 5(a) shows the cross-section of an optimized weave that was subjected to non-pressurized aluminization. Comparison with Figures 3 and 4 shows the much more open structure achieved by removal of individual wires. A NiAl shell is formed on every single wire in the weave; however, there is a significant difference at the coating thicknesses from layer to layer, as seen in Figures 5(b) through (d). The average shell thickness is $12.8 \pm 1.2 \mu\text{m}$, dropping from a thickness of 14 μm at the surface layers (#1 and #6) to 11.5 μm at the central layers (#3 and #4). Although the difference is not as substantial as it was with the standard weave, it is apparent that the gas penetration is still an issue even with the more open architecture of the optimized structure. Figure 5(b) shows two fill wires bonded to the upper warp layer, with a bond length of 75 μm . Similar to the bond seen in Figure 4(d), there is a small gap at the center of the bond. Again sharp cusps are present.

Figure 6(a) demonstrates the effect of pressurized aluminization on the optimized structures. Unlike the

non-pressurized sample (Figure 5), very uniform NiAl shells were observed on all wires, regardless of their position within the weave, as illustrated in Figures 6(b) through (d). The average coating thickness is $9.6 \pm 0.3 \mu\text{m}$. As evidenced by the smaller error value, the coating uniformity significantly improved with pressure aluminization. In Figure 6(c) two wires seem to be almost bonded, however, the initial spacing between the wires was too large to allow contact and merging of the coatings.

One common observation for all the samples is that the coatings have a rough surface appearance as seen in metallographic images. This might have two possible explanations. First is the formation of Kirkendall vacancies and pores^[36] and their migration to the surface. Goward and Boone^[24] reported that the dominant mechanism for the formation of NiAl coatings is the outward diffusion of Ni atoms, which results in surface roughening.^[37] A similar observation was previously reported by Janssen and Rieck^[38] in their work with Ni-Al diffusion couples and in our earlier work^[27] on pack-aluminized Ni and Ni-20Cr wires. The second explanation hinges on the fact that the nickel aluminides are very brittle at room temperature and surface roughening might be the result of metallographic sample preparation. It is likely that both of these factors have contributed to final surface finish. In certain applications where smooth surface is required, a final etching step could be carried out. On the other hand, roughen-

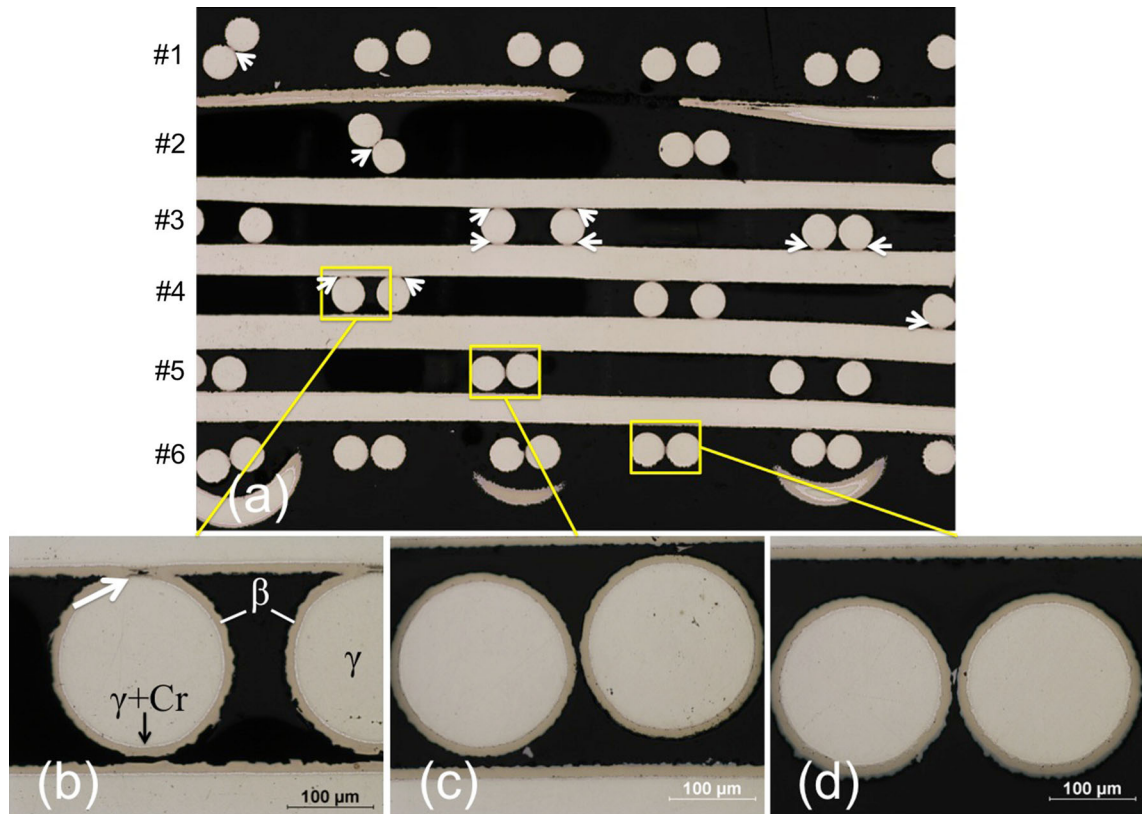


Fig. 5—(a) Optimized woven structure after non-pressurized aluminization at 1273 K (1000 °C) for 1 h, (b through d) showing higher magnification images of wires in various regions of the sample, where β -NiAl coating has a uniform thickness. An α -Cr rejection layer is present at the β -NiAl/ γ -Ni-20Cr interface. Wire bonding is observed in (b) where NiAl coatings on fill and warp wires merged during their growth. A small gap is visible at the center of the bond.

ing would increase the wire surface area and help transition from laminar to turbulent flow, which would be desirable to improve heat transfer properties.

Following the coating process, select samples were homogenized in order to obtain uniform Ni-Cr-Al compositions. One concern is the possibility of non-uniform compositions at the bonding regions, if the coating does not cover the whole circumference of the wires under certain conditions, as represented in Figure 5(b) and marked with an arrow. However, this concern was alleviated after more than ten EDS linescans from various homogenized samples revealed that the composition was completely uniform, as demonstrated in Figure 7.

Subsequent to homogenization, two samples within the γ/γ' composition range were aged at 1173 K (900 °C) for 8 hours. Figure 8 shows representative precipitate microstructure of an optimized weave that was subjected to pressurized aluminization. This sample had an overall composition of Ni-19Cr-3.4Al-1Si. The precipitates had a unimodal cuboidal morphology with a volume fraction of 22 pct and an average particle size of 153 ± 29 nm, as determined by image analysis. In a previous study with individual wires,^[27] a wire (143 μ m initial diameter) with a composition of Ni-19Cr-4.5Al-1Si had a γ' volume fraction of ~ 15 pct and an average precipitate size of 220 ± 42 nm under identical processing conditions. In the same study,

another wire with a composition of Ni-19Cr-8Al-1Si had a β -NiAl coating shell and a γ/γ' core due to over-aluminization. In the γ/γ' core, the γ' volume fraction was ~ 22 pct. The results obtained in this study with the woven structures and the ones obtained in the previous work with the individual wires are comparable within the error limits. High volume fraction of γ' precipitates are expected to provide good creep resistance, and the presence of both Al and Cr will create a protective layer against oxidation and/or corrosion at high temperatures. The pack cementation technique is suitable for the addition of other elements relevant to superalloys as well, such as Ti,^[39,40] Mo,^[41] Fe,^[22,42] and Co.^[43]

C. Hardness Evolution During the Process

Hardness values of individual wires within the weaves were measured at various stages within the process by indentation of at least five radial wire cross-sections in each layer; an estimate (in MPa) of the ultimate tensile strength (UTS) is given by tripling the Vickers hardness value, as widely used for a variety of metals including pure nickel.^[44]

Individual, as-received Ni-20Cr wires, which were annealed at 1473 K (1200 °C) for 1 hour, had a hardness value of 200 ± 11 HV (600 ± 33 MPa), which is, as expected, higher than the reported value of 160 HV

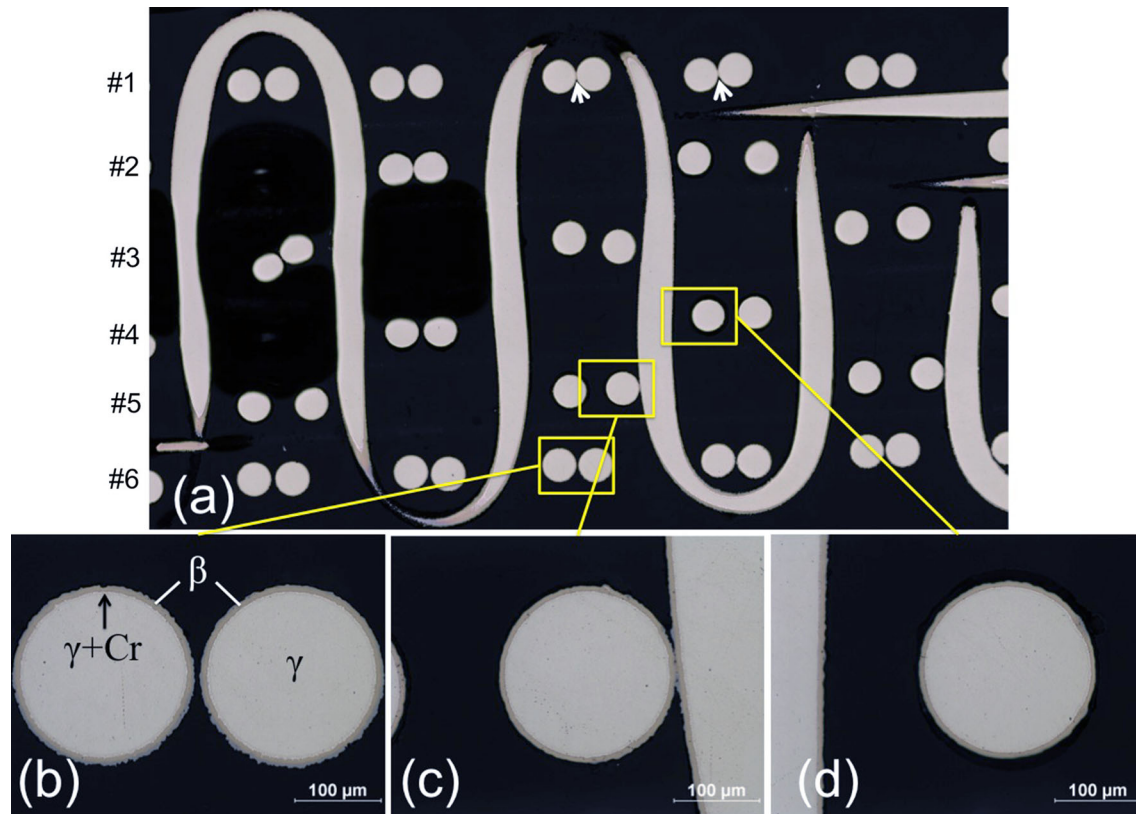


Fig. 6—(a) Optimized woven structure pressure aluminized at 1273 K (1000 °C) for 1 h, (b through d) showing higher magnification images of wires in various regions of the sample, where β -NiAl coating has a uniform thickness. An α -Cr rejection layer is present at the β -NiAl/ γ -Ni-20Cr interface. A bond between fill and Z wires was almost formed in (c), however, the initial spacing between the wires was too large for the NiAl coatings to merge.

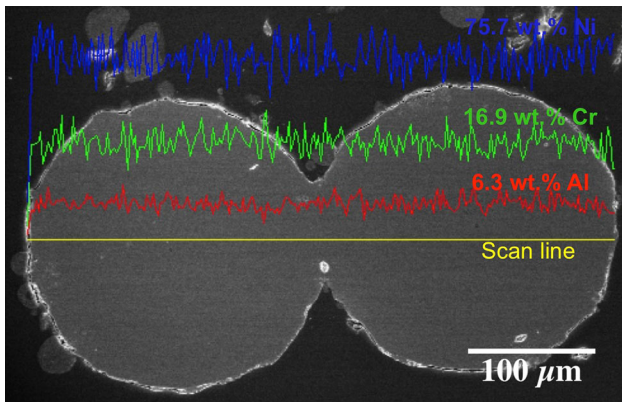


Fig. 7—EDS linescan acquired across the yellow line showing uniform distribution of Ni, Cr, and Al in a homogenized Ni-Cr-Al weave with an optimized structure. Overall composition, as measured on a non-pressure aluminized optimized weave, is Ni-16.9Cr-6.3Al-1Si-0.1Fe (wt percent).

(480 MPa) for a Cr-leaner Ni-16Cr alloy in bulk form.^[45]

Compositional differences in a non-pressure aluminized optimized woven structure were also apparent in the hardness results. A homogenized sample showed wires with a hardness of 335 ± 24 HV (1005 ± 72 MPa) at the surface layers (#1 and #6) which dropped to 285 ± 15 HV (855 ± 45 MPa) at the central layers (#3

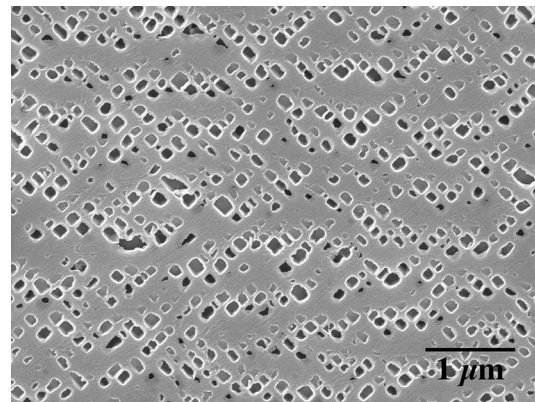


Fig. 8—Etched γ/γ' microstructure in an optimized woven structure which was pressure aluminized at 1273 K (1000 °C) for 1 h, homogenized at 1473 K (1200 °C) for 48 h, and aged at 1173 K (900 °C) for 8 h. Near-unimodal cuboidal precipitates have a volume fraction of 22 pct and an average size of 153 nm.

and #4). Another weave with an optimized architecture, pressure aluminized this time, with a uniform composition of Ni-19Cr-4Al-1Si (wt percent) had an average hardness of 276 ± 13 HV (828 ± 39 MPa) after homogenization, where SEM observations did not reveal any γ' precipitates.

This increase in hardness from the 200 ± 11 HV (600 ± 33 MPa) value for Al-free Ni-20Cr wires thus

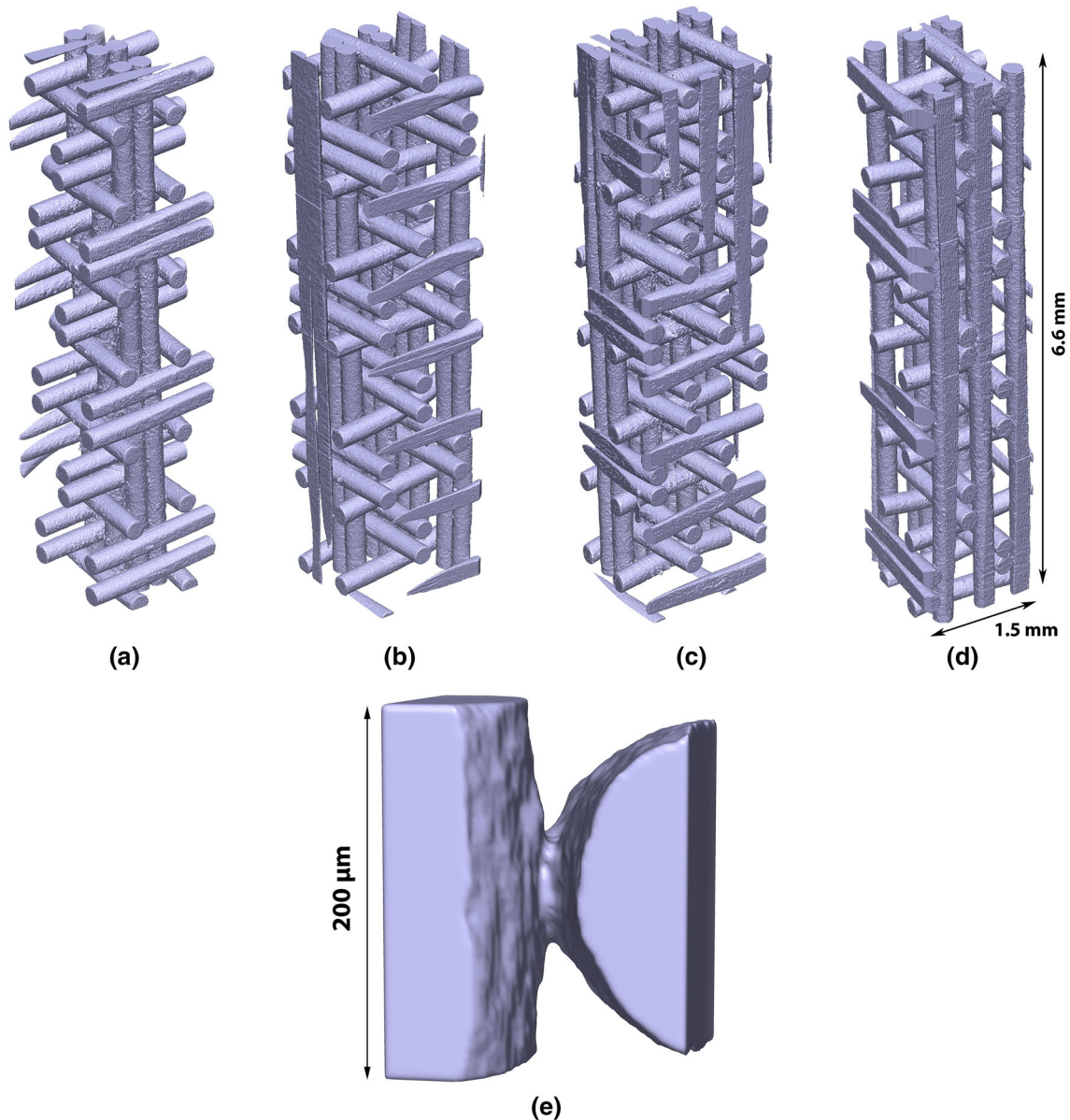


Fig. 9—Reconstructions of X-ray tomography datasets for each weave type. (a) 6 wt pct Al non-homogenized, (b) 6 wt pct homogenized, (c) 8 wt pct non-homogenized, (d) 8 wt pct homogenized, and (e) high magnification image of two bonded wires.

corresponds to solid solution strengthening. Upon aging, the hardness increased to 318 ± 24 HV (954 ± 72 MPa) in agreement with the expected precipitation strengthening, despite a drop of 0.5 wt pct Al due to evaporation during the aging treatment. This result is comparable to the one obtained with individual wires with a composition of Ni-19Cr-5Al-1Si (wt pct) and a hardness value of 320 ± 18 HV (960 ± 48 MPa).^[27]

D. Bond Quantification from Micro-tomography

Figure 9 shows the 3D tomographic reconstructions for the four optimized weave conditions, having either 6 or 8 wt pct Al before and after homogenization. Bonding between different wire types (*i.e.*, warp-to-fill, warp-to-Z, and fill-to-Z) was quantified both manually and

computationally. Manual bond identification was performed by inspection of the reconstructed slices before segmentation. Wire joints were classified as bonded, not bonded, or possibly bonded, and these results are plotted in the left-hand column of Figure 10. This method is both labor-intensive and potentially biased, motivating the development of an algorithm to automate bonding efficiency.

The algorithm needs to calculate the bonded wires as well as neighboring wires that have the potential to bond but do not contact to determine the bonding efficiency (*i.e.*, the fraction of joints bonded). This involved identifying each individual wire, assigning a wire type (fill, warp, or Z), and evaluating the number of actual and potential contacts. To identify the individual wires, the binary 3D images of the component wires were

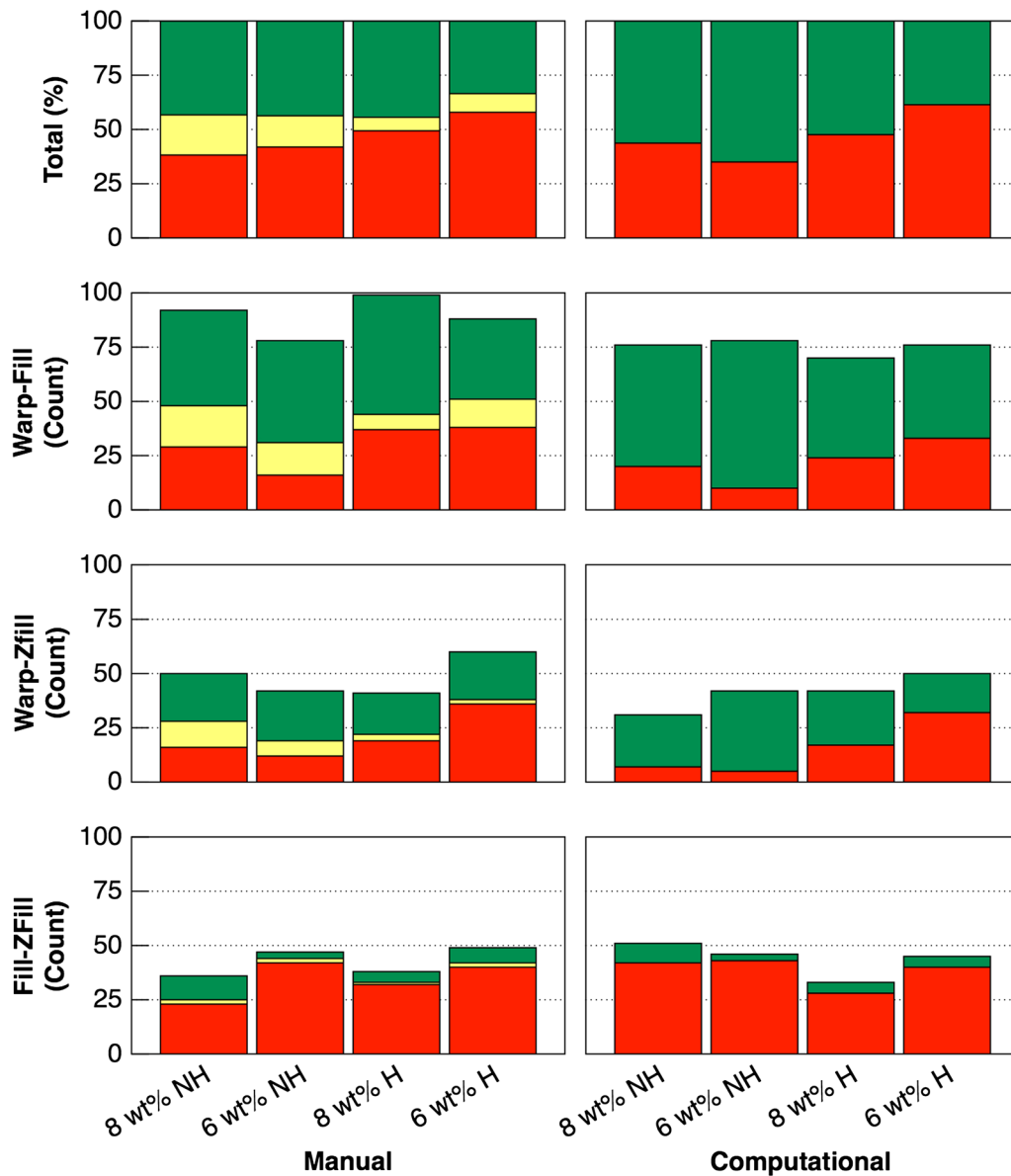


Fig. 10—Bond quantification of each sample type as determined from both manual and computational counting procedures. Red represents non-bonded wires, yellow is indeterminate, and green represents bonded wire junctions (Color figure online).

processed through a series of morphological erosion operations until all wires became separated. Wires within each sample were reduced from a starting diameter of $\sim 220 \mu\text{m}$, depending on the degree of aluminization, to a diameter of 60 to $80 \mu\text{m}$ (30 to 35 pct of the original diameter). This degree of erosion removed all wire–wire contacts in the 3D image, leaving only the center, or cores, of the original wires. A standard image-labeling algorithm was then used to assign each wire core a unique identifier. Next, each wire was assigned a type (*i.e.*, warp, fill or Z) by fitting an ellipsoid to each wire core, and using the axis of the principle inertia to specify the orientation of the wire. The wire was then assigned a wire type identifier according to the closest pre-determined wire type

orientation. Finally, the number of actual and potential contacts was evaluated. Using the unique and type identifiers, all pairs between different wire types were identified. Each unique pair of wire cores was segmented from the structure and dilated to their original diameter. If the two wires overlapped after dilation, then this interaction was counted as a bond. Wire pairs that were not bonded were then evaluated to determine if they were in close enough proximity to count as a potential bond (*i.e.*, the wire pair were neighbors that, in an ideal weave containing all contacts, would be bonded). To evaluate this, each wire of the pair was dilated an additional $80 \mu\text{m}$ beyond their original diameter to a final diameter of $\sim 380 \mu\text{m}$. If these dilated wires overlapped, they were included in the total bond count,

which includes wires that are actually bonded and neighbors that should be bonded. This is iterated through all unique wire pairs to compute the bonding efficiency (*i.e.*, the fraction of joints bonded). The results are shown in Figure 10 wherein the manual counting is displayed in the left column, and the computational results are shown in the right column. The bonding efficiency is classified by bond type interactions (warp–fill, warp–Z, and fill–Z) as well as the total for all bond types, which is represented in the top row as a percentage.

Figure 10 demonstrates that this aluminization process produced an average bonding efficiency on all four weave conditions of ~50 pct; therefore, about half of all the joints present in the structure were bonded. Some important trends between different bond types and samples emerged. First, the most efficient bonding was observed between the warp–fill wires and warp–Z wires, while bonding between fill and Z wires (bottom row in Figure 10) was quite poor. From the bending of the Z wires in the weave, it is expected that these two wire types would exhibit the lowest bonding efficiency. Bending of the Z wires causes them to be inclined relative to the weave normal direction. This inclined orientation of the Z wires along the warp direction affects bonding with the fill wires, but does not impact bonding to the warp wires. Second, the total bonding from manual quantification in Figure 10 shows that there is a slightly higher bond efficiency with the 8 wt pct Al over the 6 wt pct Al sample and a higher bonding efficiency in the non-homogenized over the homogenized weaves. Achieving greater bonding efficiency with an increase in mass gain from 6 to 8 wt pct Al would be expected as this is expected to grow the diameter of the wires.

To achieve the highest stiffness with the woven structures, bonding efficiency must be close to 100 pct. The aluminization process provides an average of 50 pct bonding efficiency, which can be increased by applying liquid phase sintering techniques. In-situ transient liquid phase bonding created by cementation deposition or deposition of commercial brazing powders, such as Ni–B, can be used.

Overall, the trends of bonding between the different weave conditions remain consistent between both measurement approaches; however, when comparing the manual and computational bond counts, discrepancies in the number of each bond type is observed with the computational approach typically undercounting the total number of bonds. These reduced counts are due to the treatment of edge wires in the computational approach. By eroding the wires to remove all wire–wire contacts, edge wires that were smaller than the erosion threshold were removed completely. All bonds with these edge wires were not counted in the automated approach, but were counted in the manual approach. For the small sample sizes used to minimize beam hardening, this resulted in a smaller number of wire interactions in the automated approach. The reduced statistics for this computational approach resulted in a lower total bonding efficiency of the 8 wt pct Al non-

homogenized sample than for the 6 wt pct sample (see Figure 10), in contradiction to expectations. This is likely due to a combination of factors that can skew these results. Namely, this dataset possessed a greater number of Z wires, a total of 21, while the other datasets have 14 resulting in a greater number of fill–Z bonds that have been shown to exhibit poor bonding. Also, this dataset contained large number of edge wires, lowering the total counts of both the warp–fill and warp–Z wires as compared to the manual approach. This points to an essential issue regarding the sample volumes evaluated in this work, specifically when dealing small analysis volumes, small variations in how the samples were sectioned from the structure can have a noticeable influence on the counting statistics. As future dataset sizes increase, the effect of edge errors will decrease, while errors from manual counting will tend to increase.

IV. CONCLUSIONS

Ni-20Cr 3D-textiles were fabricated with three different micro-architectures: braided tube, standard weave where all wire positions were filled, and optimized weave where alternating fill and warp positions were left empty. Samples pack-aluminized for 1 hour at 1273 K (1000 °C) by non-pressurized or pressurized pack cementation achieved an average composition of 3 to 5 wt pct Al, within the γ/γ' range for this alloy. Non-pressurized aluminization resulted in thicker NiAl coatings on wires near the surface than deeper within the weave, especially in the standard woven structures, because of non-uniform gas penetration through the dense structure. Pressurized aluminization solved this problem by increasing the internal pressure of the halide gas within the retort and allowing it to penetrate through the woven structure; samples with uniform NiAl coatings on all wires were achieved.

The wire composition was homogenized at Ni-19Cr-4Al-1Si (wt pct), resulting in the dissolution of the coating into the wire and the disappearance of Al composition gradients. A homogenized weave, with an average hardness of 276 HV was subsequently aged at 1173 K (900 °C) for 8 hours resulting in a hardness increase to 318 HV. This was explained by the appearance of cuboidal γ' precipitates, with a volume fraction of 22 pct and an average size of 153 ± 29 nm, which provide high creep resistance to nickel-based superalloys.

The bonding efficiency of four optimized weave conditions after pack aluminization was quantified both manually and computationally from three-dimensional datasets produced using X-ray micro-computed-tomography. It was found that this aluminization process produced an average bonding efficiency on all four weave conditions of ~50 pct, *i.e.*, about half of all the joints present in the structure were bonded. The most efficient bonding was observed between the warp–fill wires and warp–Z wires due to the geometry of the weave.

ACKNOWLEDGMENTS

The authors acknowledge the financial support from the Defense Advanced Research Projects Agency under award number W91CRB1010004 (Dr. Judah Goldwasser, program manager). They also thank Profs. Kevin Hemker, Timothy Weihs, and James Guest (Johns Hopkins University) for useful discussions, and Dr. Andrew Geltmacher (NRL) for his help with X-ray micro-tomography.

REFERENCES

1. R. Lakes: *Nature*, 1993, vol. 361, pp. 511–15.
2. H.N.G. Wadley: *Philos. Trans. R. Soc. A*, 2006, vol. 364, pp. 31–68.
3. H.N.G. Wadley, N.A. Fleck, and A.G. Evans: *Compos. Sci. Technol.*, 2003, vol. 63, pp. 2331–43.
4. N.A. Fleck, V.S. Deshpande, and M.F. Ashby: *Proc. R. Soc. A*, 2010, vol. 466, pp. 2495–2516.
5. T.A. Schaedler, A.J. Jacobsen, A. Torrents, A.E. Sorensen, J. Lian, J.R. Greer, L. Valdevit, and W.B. Carter: *Science*, 2011, vol. 334, pp. 962–65.
6. J.-H. Lim and K.-J. Kang: *Mater. Trans.*, 2006, vol. 47, pp. 2154–60.
7. Y.-H. Lee, B.-K. Lee, I. Jeon, and K.-J. Kang: *Acta Mater.*, 2007, vol. 55, pp. 6084–94.
8. Y. Brechet and J.D. Embury: *Scripta Mater.*, 2013, vol. 68, pp. 1–3.
9. M. Ashby: *Scripta Mater.*, 2013, vol. 68, pp. 4–7.
10. A.G. Evans, J.W. Hutchinson, N.A. Fleck, M.F. Ashby, and H.N.G. Wadley: *Prog. Mater. Sci.*, 2001, vol. 46, pp. 309–27.
11. L. Valdevit, A.J. Jacobsen, J.R. Greer, and W.B. Carter: *J. Am. Ceram. Soc.*, 2011, vol. 94, pp. 1–20.
12. J.K. Guest and J.H. Prevost: *Int. J. Solids Struct.*, 2006, vol. 43, pp. 7028–47.
13. V.J. Challis, J.K. Guest, J.F. Grotowski, and A.P. Roberts: *Int. J. Solids Struct.*, 2012, vol. 49, pp. 3397–3408.
14. S. Ha and J.K. Guest: Unpublished Research, Johns Hopkins University, Baltimore, MD, 2014.
15. M.V. Nathal, J.D. Whittenberger, M.G. Hebsur, P.T. Kantzos, and D.L. Krause: in *Superalloys 2004*, eds., K.A. Green, T.M. Pollock, H. Harada, T.E. Howson, R.C. Reed, J.J. Schirra, and S. Walston, TMS, 2004, pp. 431–39.
16. Q.M. Zhang and X.D. He: *Mater. Charact.*, 2009, vol. 60, pp. 178–82.
17. L. Murr, S. Li, Y. Tian, K. Amato, E. Martinez, and F. Medina: *Materials*, 2011, vol. 4, pp. 782–90.
18. D.E. Burns, Y. Zhang, M. Teutsch, K. Bade, J. Aktaa, and K.J. Hemker: *Scripta Mater.*, 2012, vol. 67, pp. 459–62.
19. A.M. Hodge and D.C. Dunand: *Intermetallics*, 2001, vol. 9, pp. 581–89.
20. H. Choe and D.C. Dunand: *Acta Mater.*, 2004, vol. 52, pp. 1283–95.
21. Q. Pang, G.H. Wu, Z.Y. Xiu, G.Q. Chen, and D.L. Sun: *Mater. Sci. Eng. A*, 2012, vol. 534, pp. 699–706.
22. Q. Pang, Z.Y. Xiu, G.H. Wu, L.T. Jiang, D.L. Sun, and Z.L. Hu: *J. Mater. Process. Technol.*, 2012, vol. 212, pp. 2219–27.
23. E.G. Gilson: *Process of Treating Metals*, US 1,091,057, US Patent Office, 1913.
24. G.W. Goward and D.H. Boone: *Oxid. Met.*, 1971, vol. 3, pp. 475–95.
25. D.K. Das, V. Singh, and S.V. Joshi: *Metall. Mater. Trans. A*, 1998, vol. 29A, pp. 2173–88.
26. S.J. Johnson, B. Tryon, and T.M. Pollock: *Acta Mater.*, 2008, vol. 56, pp. 4577–84.
27. D. Erdeniz and D.C. Dunand: *Intermetallics*, 2014, vol. 50, pp. 43–53.
28. F.K. Ko: in *Engineered Materials Handbook*, T.J. Reinhart, ed., ASM International, Metals Park, OH, 1987, pp. 519–28.
29. F.K. Ko: *Am. Ceram. Soc. Bull.*, 1989, vol. 68, pp. 401–14.
30. T.D. Kostar and T.-W. Chou: in *3-D Textile Reinforcements in Composite Materials*, A. Miravete, ed., Woodhead Publ. Ltd., Cambridge, England, 1999, pp. 217–40.
31. D. Mungalov and A.E. Bogdanovich: *SAMPE J.*, 2004, vol. 40, pp. 7–20.
32. A.E. Bogdanovich and D. Mungalov: in *Proceedings of the International Composites Conference ACUN-4*, S. Bandyopadhyay, ed., Sydney, Australia, 2002, pp. 61–72.
33. D. Mungalov and A.E. Bogdanovich: *Automated 3-D Braiding Machine and Method*, US 6,439,096, US Patent Office, 2002.
34. L.A. Feldkamp, L.C. Davis, and J.W. Kress: *J. Opt. Soc. Am. A*, 1984, vol. 1, pp. 612–19.
35. M.L. Comer and E.J. Delp: *IEEE Trans. Image Process.*, 2000, vol. 9, pp. 1731–44.
36. A.D. Smigelskas and E.O. Kirkendall: *Trans. Am. Inst. Min. Metall. Eng.*, 1947, vol. 171, pp. 130–42.
37. D.C. Tu and L.L. Seigle: *Thin Solid Films*, 1982, vol. 95, pp. 47–56.
38. M.M.P. Janssen and G.D. Rieck: *Trans. Metall. Soc. AIME*, 1967, vol. 239, pp. 1372–85.
39. M. Britchi, N. Ene, M. Olteanu, E. Vasile, P. Nita, and E. Alexandrescu: *Defect Diffus. Forum*, 2010, vols. 297–301, pp. 1–7.
40. F.S. Nogarani, F. Ashrafzadeh, and A. Saatchi: *Surf. Coat. Technol.*, 2012, vol. 210, pp. 97–102.
41. J. Li, C.Q. Xia, and Y. Gu: *J. Cent. South Univ. Technol.*, 2004, vol. 11, pp. 15–18.
42. G.X. Hu, Z.X. Xu, J.J. Liu, and Y.H. Li: *Surf. Coat. Tech.*, 2009, vol. 203, pp. 3392–97.
43. D. Schmidt, M. Galetz, and M. Schutze: *Oxid. Met.*, 2013, vol. 79, pp. 589–99.
44. D. Tabor: *J. Inst. Met.*, 1951, vol. 79, pp. 1–18.
45. F.T. Louis: *Smithells Metals Reference Book*, ed. E.A. Brandes, Butterworth & Co Ltd., England, 1983, pp. 22–69.